Draft version August 15, 2014
Preprint typeset using LaTeX style emulateapj v. 5/2/11

HOW MUCH CAN ^{56}NI BE SYNTHESIZED BY MAGNETAR MODEL FOR LONG GAMMA-RAY BURSTS AND HYPERNOVAE?

Yudai Suwa[1,2] and Nozomu Tominaga[3,4]

Draft version August 15, 2014

ABSTRACT

A rapidly rotating neutron star with strong magnetic fields, called magnetar, is a possible candidate for the central engine of long gamma-ray bursts and hypernovae (HNe). We solve the evolution of a shock wave driven by the wind from magnetar and evaluate the temperature evolution, by which we estimate the amount of ^{56}Ni that would produce a bright emission of HNe. We obtain a constraint on the magnetar parameters, namely the poloidal magnetic field strength (B_p) and initial angular velocity (Ω_i), for synthesizing enough ^{56}Ni mass to explain HNe ($M_{^{56}\mathrm{Ni}} \gtrsim 0.2 M_\odot$), i.e. $(B_p/10^{16}\ \mathrm{G})^{1/2}(\Omega_i/10^4\ \mathrm{rad\ s^{-1}}) \gtrsim 1$.

Subject headings: gamma-ray burst: general — stars: neutron — stars: winds, outflows — supernovae: general

1. INTRODUCTION

The central engine of gamma-ray bursts (GRBs) is still unknown nevertheless a wealth of observational data. The most popular scenario for a subclass with long duration (long GRB) is the collapsar scenario (Woosley 1993), which contains a black hole and a hyper accretion flow, and one of the alternatives is a rapidly rotating neutron star (NS) with strong magnetic fields ("magnetar") scenario (Usov 1992). Their energy budgets are determined by the gravitational binding energy of the accretion flow for the former scenario and the rotational energy of a NS for the latter scenario.

On the other hand, the association between long GRBs and energetic supernovae, called hypernovae (HNe), is observationally established since GRB 980425/SN 1998bw and GRB 030329/SN 2003dh (see Woosley & Bloom 2006; Hjorth & Bloom 2012, and references therein). The explosion must involve at least two components; a relativistic jet, which generates a gamma-ray burst, and a more spherical-like non-relativistic ejecta, which is observed as a HN. One of observational characteristics of HNe is high peak luminosity; HNe are typically brighter by $\sim 1-2$ mag than canonical supernovae. The brightness of HNe stems from an ejection of a much larger amount of ^{56}Ni (0.2 – 0.5 $M_\odot$; Nomoto et al. 2006) than canonical supernovae ($\lesssim 0.1 M_\odot$, e.g., Blinnikov et al. 2000 for SN 1987A).

Mechanisms that generate such a huge amount of ^{56}Ni by a HN have been investigated (e.g. MacFadyen & Woosley 1999; Nakamura et al. 2001b,a; Maeda et al. 2002; Nagataki et al. 2006; Tominaga et al. 2007; Maeda & Tominaga 2009). They demonstrated that the large amount of ^{56}Ni can be synthesized by explosive nucleosynthesis due to the high explosion energy of a HN and/or be ejected from the accretion disk via disk wind. However, no study on the ^{56}Ni mass for the magnetar scenario has been done so far. The dynamics of outflow from magnetar is investigated in detail and it is suggested that the energy release from the magnetar could explain the high explosion energy of HNe (e.g. Thompson et al. 2004; Komissarov & Barkov 2007; Dessart et al. 2008; Bucciantini et al. 2009; Metzger et al. 2011). Therefore, there is a need to study the amount of ^{56}Ni generated by magnetar central engine in order to check the consistency of this scenario.

In this Letter, we evaluate the amount of ^{56}Ni by the rapidly spinning magnetar. To do this, we adopt a thin shell approximation and derive an evolution equation of a shock wave driven by the magnetar dipole radiation. The solution of this equation gives temperature evolution of post-shock layer. Using the critical temperature (5×10^9 K) for nuclear statistical equilibrium at which ^{56}Ni is synthesized, we give a constraint on the magnetar spin rate and dipole magnetic field strength for explaining the observational amount of ^{56}Ni in HNe. In Section 2, we give expressions for the dipole radiation from a rotating magnetized neutron star for the central engine model. Section 3 is devoted to the derivation of the evolution equation of a shock wave and its solution. Based on the solution, we evaluate the temperature evolution and ^{56}Ni mass ($M_{^{56}\mathrm{Ni}}$) as a function of magnetar parameters. We summarize our results and discuss their implications in Section 4.

2. MAGNETAR EVOLUTIONS

In this section, we derive the luminosity of dipole radiation from rapidly rotating NSs. According to Shapiro & Teukolsky (1983), the luminosity of dipole radiation is given as

$$L_w = \frac{B_p^2 R^6 \Omega^4 \sin^2\alpha}{6c^3}, \tag{1}$$

where B_p is the dipole magnetic filed strength, R is the NS radius, Ω is the angular velocity, and α is the angle

[1] Yukawa Institute for Theoretical Physics, Kyoto University, Oiwake-cho, Kitashirakawa, Sakyo-ku, Kyoto, 606-8502, Japan
[2] Max-Planck-Institut für Astrophysik, Karl-Schwarzschild-Str. 1, D-85748 Garching, Germany
[3] Department of Physics, Faculty of Science and Engineering, Konan University, 8-9-1 Okamoto, Kobe, Hyogo 658-8501, Japan
[4] Kavli Institute for the Physics and Mathematics of the Universe (WPI), The University of Tokyo, Kashiwa, Chiba 277-8583, Japan

between magnetic and angular moments. Hereafter we assume $\sin\alpha = 1$ for simplicity. Then, the luminosity is expressed as

$$L_w = 6.18\times10^{51}\mathrm{erg\ s^{-1}} \times \left(\frac{B_p}{10^{16}\ \mathrm{G}}\right)^2 \left(\frac{R}{10\ \mathrm{km}}\right)^6 \left(\frac{\Omega}{10^4\ \mathrm{rad\ s^{-1}}}\right)^4. \quad (2)$$

The time evolution of the angular velocity is given as

$$\Omega(t) = \Omega_i \left(1+\frac{t}{T_d}\right)^{-1/2}, \quad (3)$$

where Ω_i is the initial angular velocity and T_d is spin down timescale given by

$$T_d = \frac{3Ic^3}{B_p^2R^6\Omega_i^2} = 8.08\ \mathrm{s}\left(\frac{B_p}{10^{16}\ \mathrm{G}}\right)^{-2}\left(\frac{R}{10\ \mathrm{km}}\right)^{-6} \times \left(\frac{\Omega_i}{10^4\ \mathrm{rad\ s^{-1}}}\right)^{-2}\left(\frac{I}{10^{45}\ \mathrm{g\ cm^2}}\right), \quad (4)$$

where I is the moment of inertia of a NS. Therefore, $L_w(t) \propto (1+t/T_d)^{-2}$. The available energy is the rotation energy of a NS,

$$E_{\rm NS} = \frac{1}{2}I\Omega_i^2 = 5\times10^{52}\ \mathrm{erg}\left(\frac{I}{10^{45}\ \mathrm{g\ cm^2}}\right)\left(\frac{\Omega_i}{10^4\ \mathrm{rad\ s^{-1}}}\right)^2, \quad (5)$$

which corresponds to the total radiation energy $E_w = \int_0^\infty L_w(t)dt = L_w(0)T_d$.

3. SHOCK EVOLUTIONS

In this section we calculate the time evolution of the shock. For simplicity, we employ thin shell approximation for the ejecta. The equation of motion of the shell is given as

$$\frac{d}{dt}\left(M_s\dot{R}_s\right) = 4\pi R_s^2 p, \quad (6)$$

where R_s is the shock radius, M_s is mass inside the shell, and p is the pressure driving the shell. $\dot{R}_s$ denotes the derivative of R_s with respect to time. The energy conservation is given as

$$\frac{d}{dt}\left(\frac{4\pi}{3}R_s^3\frac{p}{\gamma-1}\right) = L_w - p\frac{d}{dt}\left(\frac{4\pi}{3}R_s^3\right), \quad (7)$$

where γ is the adiabatic index and L_w is the wind driven by the magnetar, which is assumed to be the dipole radiation given by Eq. (2).

By substituting Eq. (6) into (7) and deleting p, we get

$$4\pi(\rho_0' R_s + 3\rho_0)R_s^2\dot{R}_s^3 + (12\pi\rho_0 R_s^3 + M_s)\dot{R}_s\ddot{R}_s + M_s R_s\dddot{R}_s = 3(\gamma-1)\left(L_w - 4\pi\rho_0 R_s^2\dot{R}_s^3 - M_s\dot{R}_s\ddot{R}_s\right), \quad (8)$$

where $\rho_0(r)$ is the density of the progenitor star (i.e. pre-shocked material) and $\rho_0' = d\rho_0/dr$. In this calculation, we used $\dot{M}_s = dM_s/dt = (dR_s/dt)(dM_s/dR_s) = 4\pi R_s^2\rho_0(R_s)\dot{R}_s$. For the density structure, ρ_0, we employ s40.0 model of Woosley et al. (2002), which is a Wolf-Rayet star with a mass of $8.7M_\odot$ and a radius of $0.33R_\odot$.

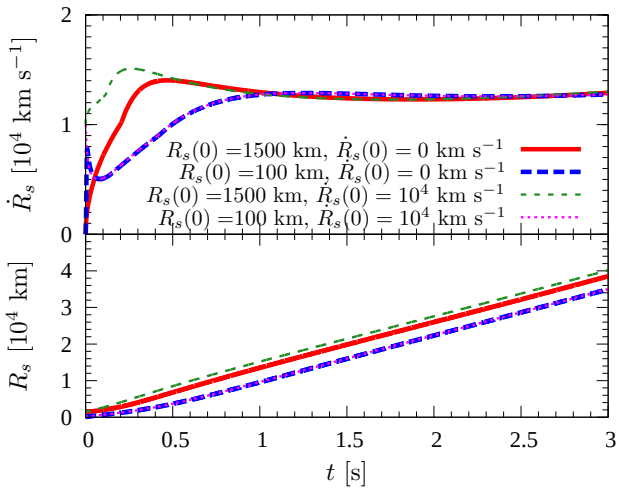

Figure 1. Time evolutions of shock velocity (top panel) and shock radius (bottom panel). Four different lines represent different initial conditions for the shock radius ($R_s(0)$ = 100 km or 1500 km) and shock velocity ($\dot{R}_s(0) = 0$ or 10^4 km s^{-1}).

In addition, we use $\gamma = 4/3$. Eq. (8) can be written to as a set of first order differential equations,

$$R_0(t) = R_s(t), \quad (9)$$
$$\dot{R}_0(t) = R_1(t), \quad (10)$$
$$\dot{R}_1(t) = R_2(t), \quad (11)$$
$$\dot{R}_2(t) = f(R_0, R_1, R_2), \quad (12)$$

where

$$f(R_0,R_1,R_2) = \frac{3(\gamma-1)}{M_sR_0}\left(L_w - 4\pi\rho_0R_0^2R_1^3 - M_sR_1R_2\right) - \frac{1}{M_sR_0}\left[4\pi(\rho_0'R_0+3\rho_0)R_0^2R_1^3 + (12\pi\rho_0R_0^3+M_s)R_1R_2\right]. \quad (13)$$

This system of differential equations is integrated using the fourth order Runge-Kutta time stepping method. Tests of this code are given in Appendix.

Figure 1 presents the time evolutions of shock radius and shock velocity for a constant luminosity of $L_w = 10^{52}$ erg s^{-1}. Three boundary conditions are needed to solve Eq. (8) because it is a third order differential equation. We set R_s, $\dot{R}_s$, and $\ddot{R}_s$ at $t = 0$. Figure 1 shows models with different initial conditions; models with different injection points $R_s(t=0) = 1500$ km (red thick-solid and green thin-dashed lines), and $R_s(0) = 100$ km (blue thick-dashed and magenta thin-dotted lines), and models with different initial velocity $\dot{R}_s(0) = 0$ (two thick lines) and 10^4 km s^{-1} (two thin lines). We find that the dependence on the initial $\ddot{R}_s$, which is 0 for all models shown in this figure, is very minor so that we do not show its dependence here. In these calculations, $M_s(t=0) = 0$, i.e. the mass below $R_s(0)$ is assumed to be a compact object and does not contribute to the mass of the shell. For cases with $R_s(0) = 1500$ km (red thick-solid and green thin-dashed lines), the different initial velocities lead to slightly different shock evolutions. On the other hand, for cases with $R_s(0) = 100$ km (blue thick-dashed and magenta thin-dotted lines), the initial velocity does not change the later shock evolution at all. The almost con-

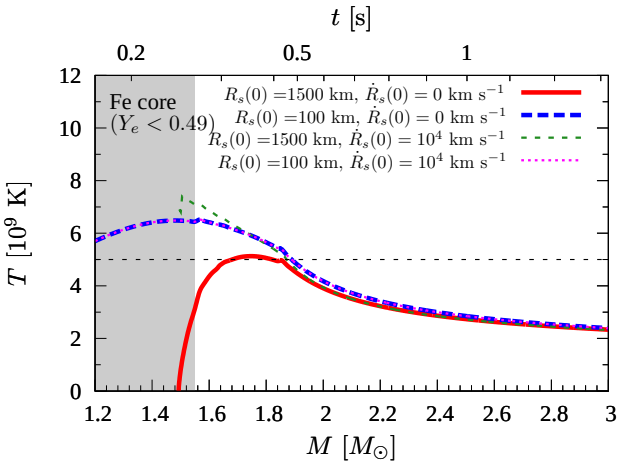

Figure 2. The postshock temperature as a function of mass coordinate. The model parameters are the same as in Figure 1. The horizontal dotted line represents 5×10^9 K, above which ^{56}Ni is synthesized. The gray shaded region, $M(r) < 1.55M_\odot$, is the iron core, where ^{56}Ni cannot be synthesized due to the low electron fraction of $Y_e < 0.49$. The corresponding time of the model with $R_s(0) = 100$ km and $\dot{R}_s(0) = 0$ (blue thick-dashed line) is given on the upper axis.

stant velocity is a consequence of the density structure, $\rho_0(r) \propto r^{-\beta}$, with $\beta \approx 2$ (see Appendix for analytic solution).

Nuclear statistical equilibrium holds and ^{56}Ni is synthesized in a mass shell with the maximum temperature of $> 5 \times 10^9$ K. Thus, the temperature evolution is crucial for the amount of ^{56}Ni. In the following, we consider the postshock temperature, which is evaluated with the following equation of state,

$$p = p_i + p_e + p_r, \tag{14}$$

where $p_i = n_i k_B T$, $p_e = (7/12) a_{\rm rad} T^4 [T_9^2/(T_9^2 + 5.3)]$, and $p_r = a_{\rm rad} T^4/3$ are contributions from ions, non-degenerate electron and positron pairs (Freiburghaus et al. 1999; Tominaga 2009), and radiation, respectively. Here, $n_i = \rho/m_p$ is the ion number density with m_p being the proton mass and ρ being the density in the shell,[5] T is the temperature in the shell, $T_9 = (T/10^9$ K), k_B is Boltzmann's constant, and $a_{\rm rad} = 7.56 \times 10^{-15}$ erg cm^{-3} K^{-4} is the radiation constant. Combined with Eq. (6), we obtain T in the shell and its evolution being consistent with the shock dynamics. Figure 2 gives the temperature in the expanding shell as a function of mass coordinate for the same model as in Figure 1. The electron fraction in the iron core ($M \lesssim 1.55M_\odot$) is less than 0.49 so that no ^{56}Ni production is expected. In order to achieve $T > 5 \times 10^9$ K just above the iron core, an initially fast shock wave or a shock injected deep inside is necessary. This is because smaller initial velocity leads to a smaller initial kinetic energy, and larger injection radius leads to shorter and smaller energy injection before the shock reaches a certain radius. Therefore, we employ $R_s(0) = 100$ km and $\dot{R}_s(0) = 0$ to evaluate the *maximum* amount of ^{56}Ni in the following calculation.

[5] Note that ρ should be different from ρ_0 because matter is compressed by the shock wave. Due to our simple thin shell approximation we need an additional assumption to evaluate ρ. We hereby simply assume that $\rho = \rho_0$, which would lead to slightly higher temperature. This assumption does not drastically change the discussion of ^{56}Ni mass because the radiation pressure dominates over the matter pressure for the region interested in here. Although the pressure inside the shell might also be different from the one behind the shell, we neglect the difference for simplicity (see discussion in the Appendix).

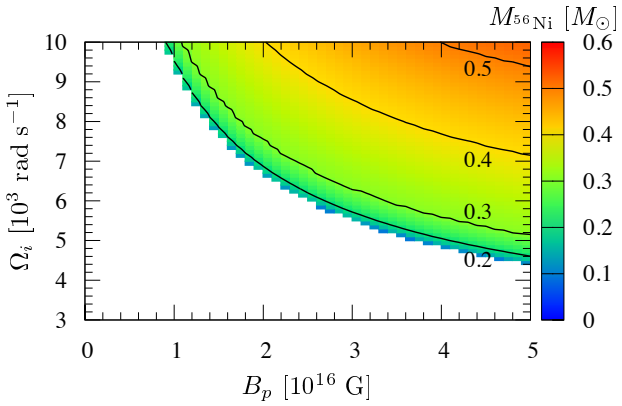

Figure 3. The amount of ^{56}Ni in units of $M_\odot$ for magnetar model as a function of the strength of the dipole magnetic field, B_p and the initial angular velocity, Ω_i. The region with $M < 1.55M_\odot$ is not included because $Y_e < 0.49$ and no ^{56}Ni production is expected there. Black solid lines represent $M_{^{56}\rm Ni}$ from 0.2 to 0.5 $M_\odot$.

Next, we consider the shock driven by the magnetar's dipole radiation given in the previous section. Figure 3 shows the ^{56}Ni mass produced in the expanding shell as a function of B_p and Ω_i. In this figure, we employ $R_{\rm NS} = 10$ km and $I = 10^{45}$ g cm^2. Here, we assume that the matter that experienced $T > 5 \times 10^9$ K is competely converted to ^{56}Ni, i.e., $X(^{56}{\rm Ni}) = 1$, except for $M(r) < 1.55M_\odot$ where ^{56}Ni cannot be synthesized due to a low electron fraction (Y_e). From this figure, we can easily see a rapid increase from 0 to $0.2M_\odot$ of $M_{^{56}\rm Ni}$ due to the progenitor structure. In this progenitor, the silicon core has a mass of $\sim 1.84M_\odot$, and in the surrounding oxygen burning layer the density slope β is different. This change in β causes the change of velocity evolution shown in Figure 1: for instance, the blue thick-dashed line represents a rapid acceleration at $t \lesssim 0.5$ s and a slow acceleration or an almost constant velocity afterwards.

Since the observed brightness of HNe requires ~ 0.2 – $0.5M_\odot$ of ^{56}Ni (Nomoto et al. 2006), a reasonable central engine model must achieve this quantity. We find that for $M_{^{56}\rm Ni} \gtrsim 0.2M_\odot$, the following relation should be satisfied;

$$\left(\frac{B_p}{10^{16}\ {\rm G}}\right)^{1/2} \left(\frac{\Omega_i}{10^4\ {\rm rad\ s^{-1}}}\right) \gtrsim 1. \tag{15}$$

Interestingly, this condition is equivalent to the constraint on the luminosity given by Eq. (2) as $L_w \gtrsim 6.2 \times 10^{51}$ erg s^{-1}. The dependence on T_d is small because $M_{^{56}\rm Ni} \sim 0.2M_\odot$ is realized when T_d is longer than the shock propagating time up to $M(r) \approx 1.75M_\odot$. Note that Eq. (15) is a conservative constraint because in this calculation we made several approximations, which always result in larger $M_{^{56}\rm Ni}$. Thus, for a more realistic case, $M_{^{56}\rm Ni}$ becomes smaller than this estimate. To make a reasonable amount to explain the observation, a more energetic central engine is needed.

In order to investigate the progenitor dependence, we

perform the same calculation with different progenitor models and find that the r.h.s. of Eq. (15) is ∼0.8 – 1.1; 1 for 20 $M_\odot$, 1.1 for 40 $M_\odot$, 0.9 for 80 $M_\odot$ models of Woosley & Heger (2007), and 0.8 for 20 $M_\odot$ model of Umeda & Nomoto (2005). Therefore, this criterion does not strongly depend on the detail of the progenitor structure.

4. SUMMARY AND DISCUSSION

In this study, we employed the thin shell approximation for the shock structure and calculated the evolution of a shock wave driven by the wind from a rapidly rotating neutron star with strong magnetic fields ("magnetar"). By evaluating the temperature evolution that is consistent with the shock evolution, we obtained a constraint on the magnetar parameters, namely the magnetic field strength and rotation velocity, for synthesizing enough amount of ^{56}Ni to explain the brightness of HNe.

In this calculation, we employed several assumptions.

- The dipole radiation is dissipated between the NS and the shock and thermal pressure drives the shock evolution. This assumption leads to larger amount of ^{56}Ni than a more realistic situation because if the conversion from Poynting flux to thermal energy is insufficient, the internal energy is smaller and the temperature in the shell is lower than the current evaluation. Therefore, the mass that experienced $T > 5 \times 10^9$ becomes smaller.
- The shock and energy deposition from the magnetar are spherical, which leads to larger ^{56}Ni mass. This is because if we concentrate all the energy in a small region, fallback of matter onto a NS takes place and reduces $M_{^{56}\mathrm{Ni}}$ (Bucciantini et al. 2009; Maeda & Tominaga 2009; Yoshida et al. 2014).
- All energy radiated by the NS is used for HN component, which is overestimated because a part of the energy should be used to make the relativistic jet component of a GRB.
- Matter which experiences $T > 5 \times 10^9$K consists only of ^{56}Ni, i.e. $X(^{56}\mathrm{Ni}) = 1$. This overestimates $M_{^{56}\mathrm{Ni}}$ because $X(^{56}\mathrm{Ni}) < 1$ even in the layer which experiences $T > 5 \times 10^9$ K according to hydrodynamical and nucleosynthesis simulations (Tominaga et al. 2007).
- The mass cut corresponds to the iron core mass, $1.55M_\odot$. If the NS mass is larger than the iron core mass, the ^{56}Ni mass becomes even smaller.

Combining these facts, our estimation of the ^{56}Ni mass is probably highly overestimated so that our constraint on the magnetar parameters (Eq. 15) is ratherconservative. Interestingly, it is still a stringent constraint; a very high magnetic field strength and a very rapid rotation are required to explain the brightness of HNe.

There have been some studies that tried to explain the plateau phase of the early afterglow by the magnetar scenario because the long lasting activity can be explained by long-living magnetars. This discriminates magnetar scenario from the collapsar scenario, whose lifetime is determined by the accretion timescale of the hyperaccretion flow. The typical values for B_p and Ω_i for long GRBs are $\gtrsim 3 \times 10^{14}$ G and $\gtrsim 6 \times 10^3$ rad s^{-1} (Troja et al. 2007) and 3.2 – 12×10^{14} G and 1.7-6.3×10^3 rad s^{-1} (Dall'Osso et al. 2011). These values are far less than those given by Eq. (15). Therefore, if these GRBs are actually driven by a magnetar, we cannot expect the bright emission of HNe generated by the decay of ^{56}Ni. When we observe a GRB, whose observational data can be explained by a magnetar with not fulfilling the constraint given by Eq. (15), and it is accompanied by a HN, we need an additional energy source to synthesize ^{56}Ni other than the dipole radiation from magnetars.

Since the magnetar scenario was recently suggested for the central engine of superluminous supernovae (SLSNe) (e.g. Kasen & Bildsten 2010; Woosley 2010; Gal-Yam 2012) as well as GRBs, our discussion is applicable to this class of explosion. For instance, Kasen & Bildsten (2010) proposed that $B_p \sim 5\times10^{14}$ G and $\Omega_i \sim 10^2 - 10^3$ rad s^{-1} are required to power the light curve of SLSNe. Thus, if the magnetar powers SLSNe, the synthesis of ^{56}Ni is not expected.

YS thanks E. Müller for comments and M. Suwa for proofreading. This study was supported in part by the Grant-in-Aid for Scientific Research (Nos. 25103511 and 23740157). YS was supported by JSPS postdoctoral fellowships for research abroad, MEXT SPIRE, and JICFuS. TN was supported by World Premier International Research Center Initiative (WPI Initiative), MEXT, Japan.

APPENDIX

A. CODE TESTS

Here, we show the validity of our code. At first, we calculate the expanding shock with a constant velocity and compare it with an analytic solution. Next, we evolve the shock driven by a thermal bomb and compare it with a hydrodynamic simulation result.

When we employ a density structure,

$$\rho(r) = \rho_c \left(\frac{r}{r_c}\right)^{-2}, \tag{A1}$$

where ρ_c and r_c are constants, together with a constant luminosity, the shock velocity becomes constant, i.e. $\ddot{R}_s = \dddot{R}_s = 0$. From Eq. (8), we can evaluate the shock velocity as

$$\begin{aligned}\dot{R}_s &= \left(\frac{L_w}{8\pi\rho_c r_c^2}\right)^{1/3} \\ &= 3.41 \times 10^8 \text{ cm s}^{-1} \left(\frac{L_w}{10^{51} \text{ erg s}^{-1}}\right)^{1/3} \\ &\quad \times \left(\frac{\rho_c}{10^{12} \text{ g cm}^{-3}}\right)^{-1/3} \left(\frac{r_c}{10^6 \text{ cm}}\right)^{-2/3}. \end{aligned} \tag{A2}$$

Figure 4 exhibits the relative error, |1−(numerical solution)/(exact solution)| of the shock velocity for a shock imposed at 1000 km with the velocity of Eq. (A2). Three lines, which show the different time steps (dt), represent that the relative error is keeping significantly small for any time. Cases with $dt = 10^{-2}$ s and 10^{-3} s are almost identical, which implies the convergence of the solution.

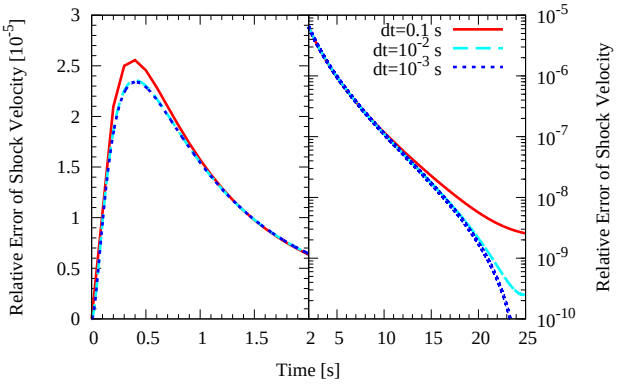

Figure 4. Absolute value of the relative error of the numerical solution for Eq. (A2). Different lines represent results with different time steps.

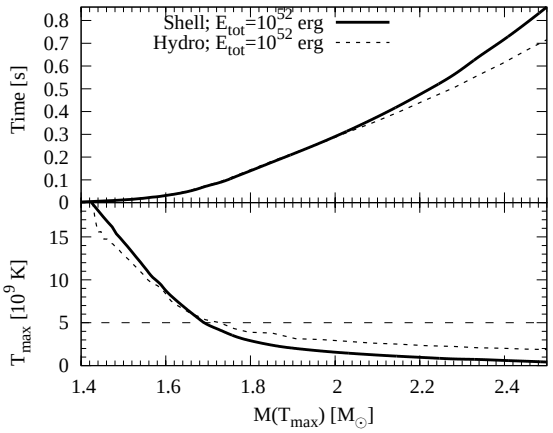

Figure 5. The passing time (top panel) and maximum temperature (bottom panel) for the shock driven by a thermal bomb as a function of mass coordinate. Solid and dotted curves represent the results of shell approximation (this work) and a hydrodynamic simulation, respectively. The horizontal dashed line in the bottom panel represents the critical temperature for ^{56}Ni synthesis, 5×10^9 K.

The remaining error comes from the discretization error of the background quantities, i.e. $\rho(r)$ and $M(r)$, which becomes smaller at late time because the error coming from $\Delta r/r$ becomes smaller due to the constant Δr (10 km). This error does not affect the discussion in this study.

Next, we compare our calculation with a hydrodynamic simulation. In this comparison, we employ a thermal bomb of 10^{52} erg to produce an explosion, injected at $M(r) = 1.35M_\odot$ of the $20M_\odot$ progenitor of Umeda & Nomoto (2005). In Figure 5, we show the comparison of the passing time (top panel) and the maximum temperature (bottom panel) as a function of mass coordinate for the shell calculation (this work) and the hydrodynamic simulation (Tominaga et al. 2007). The shock evolutions computed with these different methods agree quite well for $M(r) \lesssim 2M_\odot$ (see top panel of this figure). Above this mass, the thin shell approximation breaks down gradually and it predicts a longer propagation time than the hydrodynamic simulation, whose expanding shell has a structure. The difference in temperature is due to the crude treatment of microphysics in this calculation, in contrast to the hydrodynamical simulation including nuclear energy releases from the α network and a more realistic equation of state (Nomoto 1982; Nomoto & Hashimoto 1988). The higher temperature in the early phase is a consequence of two facts; the lower density in the shell and lacking nuclear reactions that could be endothermic at high temperature. The lower temperature in the late phase is a result of breakdown of the thin shell approximation and the lack of nuclear recombination. The systematic error of our thin shell approximation for ^{56}Ni mass is $\sim O(0.01)M_\odot$, which is smaller than the characteristic amount of ^{56}Ni of HNe, $O(0.1)M_\odot$.

REFERENCES

Blinnikov, S., Lundqvist, P., Bartunov, O., Nomoto, K., & Iwamoto, K. 2000, ApJ, 532, 1132
Bucciantini, N., Quataert, E., Metzger, B. D., et al. 2009, MNRAS, 396, 2038
Dall'Osso, S., Stratta, G., Guetta, D., et al. 2011, A&A, 526, A121
Dessart, L., Burrows, A., Livne, E., & Ott, C. D. 2008, ApJ, 673, L43
Freiburghaus, C., Rembges, J.-F., Rauscher, T., et al. 1999, ApJ, 516, 381
Gal-Yam, A. 2012, Science, 337, 927
Hjorth, J., & Bloom, J. S. 2012, The Gamma-Ray Burst - Supernova Connection, 169–190
Kasen, D., & Bildsten, L. 2010, ApJ, 717, 245
Komissarov, S. S., & Barkov, M. V. 2007, MNRAS, 382, 1029
MacFadyen, A. I., & Woosley, S. E. 1999, ApJ, 524, 262
Maeda, K., Nakamura, T., Nomoto, K., et al. 2002, ApJ, 565, 405
Maeda, K., & Tominaga, N. 2009, MNRAS, 394, 1317
Metzger, B. D., Giannios, D., Thompson, T. A., Bucciantini, N., & Quataert, E. 2011, MNRAS, 413, 2031
Nagataki, S., Mizuta, A., & Sato, K. 2006, ApJ, 647, 1255
Nakamura, T., Mazzali, P. A., Nomoto, K., & Iwamoto, K. 2001a, ApJ, 550, 991
Nakamura, T., Umeda, H., Iwamoto, K., et al. 2001b, ApJ, 555, 880
Nomoto, K. 1982, ApJ, 253, 798
Nomoto, K., & Hashimoto, M. 1988, Phys. Rep., 163, 13
Nomoto, K., Tominaga, N., Tanaka, M., et al. 2006, Nuovo Cimento B Serie, 121, 1207
Shapiro, S. L., & Teukolsky, S. A. 1983, Black holes, white dwarfs, and neutron stars: The physics of compact objects (New York, Wiley-Interscience, 1983, 663 p.)
Thompson, T. A., Chang, P., & Quataert, E. 2004, ApJ, 611, 380
Tominaga, N. 2009, ApJ, 690, 526
Tominaga, N., Maeda, K., Umeda, H., et al. 2007, ApJ, 657, L77
Troja, E., Cusumano, G., O'Brien, P. T., et al. 2007, ApJ, 665, 599
Umeda, H., & Nomoto, K. 2005, ApJ, 619, 427
Usov, V. V. 1992, Nature, 357, 472
Woosley, S. E. 1993, ApJ, 405, 273
—. 2010, ApJ, 719, L204
Woosley, S. E., & Bloom, J. S. 2006, ARA&A, 44, 507
Woosley, S. E., & Heger, A. 2007, Phys. Rep., 442, 269
Woosley, S. E., Heger, A., & Weaver, T. A. 2002, Reviews of Modern Physics, 74, 1015
Yoshida, T., Okita, S., & Umeda, H. 2014, MNRAS, 438, 3119